ARTICLE IN PRESS

Nature Communications

https://doi.org/10.1038/s41467-026-70122-x

Article in Press

Hyperparametric solitons in nondegenerate optical parametric oscillators

Received: 3 July 2025

Accepted: 18 February 2026

Cite this article as: Weng, H., Ji, X., Ali, M. *et al.* Hyperparametric solitons in nondegenerate optical parametric oscillators. *Nat Commun* (2026). https://doi.org/10.1038/s41467-026-70122-x

Haizhong Weng, Xinru Ji, Mugahid Ali, Edward H. Krock, Lulin Wang, Vikash Kumar, Weihua Guo, Qing Wan, Tobias J. Kippenberg, John F. Donegan & Dmitry V. Skryabin

We are providing an unedited version of this manuscript to give early access to its findings. Before final publication, the manuscript will undergo further editing. Please note there may be errors present which affect the content, and all legal disclaimers apply.

If this paper is publishing under a Transparent Peer Review model then Peer Review reports will publish with the final article.

ARTICLE IN PRESS

© The Author(s) 2026. **Open Access** This article is licensed under a Creative Commons Attribution 4.0 International License, which permits use, sharing, adaptation, distribution and reproduction in any medium or format, as long as you give appropriate credit to the original author(s) and the source, provide a link to the Creative Commons licence, and indicate if changes were made. The images or other third party material in this article are included in the article's Creative Commons licence, unless indicated otherwise in a credit line to the material. If material is not included in the article's Creative Commons licence and your intended use is not permitted by statutory regulation or exceeds the permitted use, you will need to obtain permission directly from the copyright holder. To view a copy of this licence, visit http://creativecommons.org/licenses/by/4.0/.

ARTICLE IN PRESS

Hyperparametric solitons in nondegenerate optical parametric oscillators

Haizhong Weng[1,2], Xinru Ji[3], Mugahid Ali[1], Edward H. Krock[1], Lulin Wang[1], Vikash Kumar[1], Weihua Guo[4], Qing Wan[2], Tobias J. Kippenberg[3], John F. Donegan[1,*] and Dmitry V. Skryabin[5,6,7,**]
[1] *School of Physics, CRANN, AMBER, and CONNECT, Trinity College Dublin, D02 PN40, Dublin 2, Ireland*
[2] *Center for Heterogeneous Integration of Functional Materials and Devices, Yongjiang Laboratory, 315202, Ningbo, China*
[3] *Institute of Physics, Swiss Federal Institute of Technology Lausanne (EPFL), CH-1015 Lausanne, Switzerland*
[4] *Wuhan National Laboratory for Optoelectronics, and School of Optical and Electronic Information, Huazhong University of Science and Technology, 430074, Wuhan, China*
[5] *Department of Physics, University of Bath, Bath, BA2 7AY, United Kingdom*
[6] *Centre for Photonics, University of Bath, Bath, BA2 7AY, United Kingdom*
[7] *National Physical Laboratory, Teddington, TW11 0LW, United Kingdom*
[*] *Corresponding author: jdonegan@tcd.ie*
[**] *Corresponding author: d.v.skryabin@bath.ac.uk*
(Dated: February 17, 2026)

ABSTRACT

Dissipative solitons and their frequency combs hold great potential for applications in optical communications, spectroscopy, precision time-keeping and beyond. Recent demonstrations based on the combination of second-harmonic generation and degenerate optical parametric oscillators (OPOs) show the interest in shifting soliton spectra away from the telecom's C-band pump sources. However, these approaches lack the tunability offered by nondegenerate OPOs. This work presents a proof-of-principle demonstration of solitons in a nondegenerate OPO system based on a silicon-nitride microresonator, with engineered dispersion and optimized coupling rates. By pumping a relatively low-Q resonance in the C-band, we excite a signal soliton comb centred around a far-detuned, high-Q, O-band resonance, as well as repetition-rate-locked combs at the pump and idler frequencies, with the latter occurring at a wavelength beyond 2 µm. The solitons supported by this platform — hyperparametric solitons — are distinct from other families of dissipative solitons, as they emerge when the narrow-band signal mode, phase-matched under negative pump detuning, reaches sufficient power to drive bistability in the parametric signal. We investigate the properties of hyperparametric solitons, including their parametrically generated background and multisoliton states, both experimentally and through theoretical modelling.

INTRODUCTION

Microresonator optical frequency combs (microcombs) have made a profound impact on modern-day nonlinear integrated photonics and revolutionised fundamental research in optical solitons [1–4]. The unique features of such microresonator combs include their compactness and high repetition rates, with potential for mass production. At the same time, dissipative solitons represent the most application-relevant class of low-noise microcombs [4]. Broadening and stabilising soliton spectra have produced some of the most exciting research directions in this area. Spectra of solitons, typically centred around the pump wavelength, can span an octave in dispersion-engineered resonators [5–7] and may be further broadened by applying a second pump that also serves to stabilise the comb repetition rates and offset frequencies [8–10], and to initiate multi-colour soliton generation [11].

The rigid attachment of the aforementioned solitons, known as dissipative Kerr solitons [4], to a specific pump wavelength, which also builds the soliton background, may also limit the comb spectral bandwidth. Expanding the spectral range of dissipative solitons into the mid-infrared region, as well as across other telecom bands, and into the visible and even UV parts of the spectrum, while still utilising the 1550 nm (C-band) pump, will enhance the impact of microcombs in telecommunications, spectroscopy, and metrology.

By utilizing nonlinear frequency conversion processes, e.g., Raman scattering, second and third harmonic generation, and parametric frequency conversion, it is possible to design microresonators that generate microcombs far away from the pump frequency. For example, Kerr solitons in silica glass microresonators that are pumped in the C-band have been shown to generate Stokes-pair solitons through the Raman effect, allowing tunability across the L and U communication bands of optical fibers [13, 14]. Multi-colour solitons and combs with two pumps in Kerr resonators have also been demonstrated [8, 9, 15]. Second-harmonic generation in thin-film lithium niobate (LN) microresonators, which exhibit a combination of strong Kerr and second-order nonlinearities, has been employed to convert C-band solitons into non-solitonic near-visible combs [16] and to demonstrate two-colour solitons [17].

Parametric frequency conversion is, however, of primary interest in the context of our work. By engineering phase-matched parametric frequency conversion relying on either $\chi^{(2)}$ or Kerr nonlinearity, one can create opti-

ARTICLE IN PRESS

ARTICLE IN PRESS

cal parametric oscillators (OPOs) generating signals far detuned from the pump frequency [18–31], see Figs. 1a,b for a conceptual illustration of both degenerate and nondegenerate Kerr OPOs. In Kerr microresonator OPOs, the parametric gain is proportional to the coupled-in, i.e., intraresonator, pump power. As the gain increases, when the pump frequency is tuned closer to the resonance, the OPO signal can start coexisting with a stable non-OPO state, see Fig. 1b. In the case of degenerate OPOs, this coexistence has been a key prerequisite for demonstrations of parametric solitons making trains of signal pulses having a zero (non-OPO) background [32–34], see Figs. 1c,d.

In particular, parametric solitons have been demonstrated using $\chi^{(2)}$ nonlinearity for parametric downconversion, from 775 nm pump to a 1550 nm signal, in an AlN microresonator [32]. A similar soliton experiment was later conducted in a fibre loop resonator, which included a short piece of $\chi^{(2)}$-active fibre for parametric gain [34]. The reference [33] used an all-Kerr Si_3N_4 microresonator with the dispersion profile phase-matched for the degenerate four-wave mixing process, $2f_{\text{signal}} = f_{\text{pump},1} + f_{\text{pump},2}$, with the pumps close to 1.0μm and 1.5μm creating parametric gain for the degenerate or near-degenerate signal photons at 1.2μm, see Figs. 1a-1d. Here and below, f's with various subscripts are used to annotate optical frequencies.

Common features of the parametric solitons observed in [32–34] were device operation near the degeneracy point, providing a zero background for soliton pulses and the coexistence of solitons with identical intensity profiles and phases differing by π [33, 34]. The zero-background property also means that the soliton central frequency does not dominate the rest of the signal comb, see Fig. 1d. This is unlike when a soliton is spectrally centred on the pump frequency and is governed by the classic form of the Lugiato-Lefever model [4].

Degenerate optical parametric oscillators (OPOs) are efficient for frequency conversion of the pump light, but they lack the tunability of nondegenerate OPOs with significant spectral separation between signal and idler, which is achieved by controlling phase matching. Indeed, in degenerate OPOs or second-harmonic generation, adjusting the phase-matching condition only controls the conversion efficiency but not the frequency of the generated signal. In recent developments, nondegenerate OPOs operating in the continuous-wave (CW) regime within microresonators and waveguides have achieved improvements in both tunability and efficiency [18–31]. However, despite the wealth of results in the CW domain, no microresonator nondegenerate OPO that generates soliton microcombs has been demonstrated to date. Our current work fills this gap by presenting a new class of dissipative optical solitons and highlighting critical differences with solitons in degenerate OPOs.

In introducing the physical concept of our work, it is natural to start by mentioning that theoretical results on bright zero-background solitons in degenerate OPOs were reported in optics as early as two decades ago [35–38], and even earlier in the contexts of fluid mechanics and condensed matter physics [39–41].

Theoretical investigations of bright solitons in nondegenerate OPO systems—where the signal and idler fields are well separated spectrally—were also conducted during this early period [42, 43]. These studies were technically and conceptually linked to the degenerate case and, therefore, found only solitons localised on a zero background, again arising in regimes where an OPO state coexists with a stable non-OPO state. Notably, we have not seen such solitons in the experiments reported below.

Here, we report a class of solitons in microresonator OPOs that have not been theoretically predicted or experimentally demonstrated. We use a Si_3N_4 resonator designed and pumped in C-band to support a nondegenerate phase-matched four-wave mixing process, $f_{\text{signal}} = 2f_{\text{pump}} - f_{\text{idler}}$, with the O-band signal near 1.25μm, and the idler near 2μm, see Fig. 1e. The resonator operates in the over-coupled regime, where the pulley coupler is designed to ensure that the coupling rate for the pump exceeds that for the signal and idler. We demonstrate that such conditions ensure that the signal not only increases with the pump but also depletes it sufficiently for the OPO state to fold on itself, creating a bistable loop between two distinct OPO states operating in the same resonator modes, see OPO-1 and OPO-2 in Fig. 1f.

Then, we experimentally and numerically demonstrate that the OPO bistability triggers the formation of signal solitons. This implies that the parametric generation does not turn off at the soliton tails since OPO-2 remains excited. This characteristic sets hyperparametric solitons apart from the parametric ones observed in degenerate OPOs, as illustrated in Figs. 1c,d and 1g,h. The term "hyperparametric solitons", which we coin here, emphasizes that parametric processes play an even more crucial role than in traditional "parametric" solitons. The latter are situated on a zero OPO background, while our solitons are based on a fully developed monochromatic parametric signal. It is worth noting that the term hyperparametric oscillations has been previously used in the context of microresonators [20, 44], but not in relation to solitons.

The frequency of parametric solitons in the degenerate $\chi^{(2)}$ OPOs is restricted to half of the pump frequency [32, 34]. Similarly, the frequency of Kerr parametric solitons hits the mid-point between the two pumps [33]. Thus, both setups are tunable only by adjusting the pump frequencies. In contrast, nondegenerate OPOs offer tuning capabilities in the range of several tens to up to 100 THz by choosing resonator geometries that provide suitable phase matching conditions [21–28, 45, 46].

ARTICLE IN PRESS

RESULTS

In this work, we used a Si_3N_4 microring resonator with a cross-section of 770 nm×2520 nm (thickness×ring width) and approximately 200 GHz repetition rate designed to provide phase-matching conditions between two identical pump TM_{00} photons with frequency around 191.4 THz and signal and idler photons close to 242.0 THz and 140.8 THz, respectively. The details for designing the phase-matching and choosing the present geometry condition can be found in the Supplementary Information (Supplementary Figs. 1a1c). The resonators were fabricated via a DUV-based subtractive approach, with the capability of wafer-scale manufacturing of Si_3N_4 photonic integrated circuits with ultra-low propagation loss and precise control of dimensions [47], see Methods. A pulley coupler with a gap of 650 nm was used to provide over-coupling for the pump, see Figs. 2a and 2b. The waveguide segment with the same curvature as the ring is approximately 50μm long, which yielded the anti-resonance coupling range around 154 THz corresponding to the drop in the coupling rate and a sharp peak in loaded quality factor (Q^{load}) [48], see the simulated result (solid curve) shown in Fig. 2d.

Available light sources allowed us to carry out the transmission measurements in two regimes that cover C-band (pump) and O-band (signal). Two transmission spectra are presented in Supplementary Information (see Supplementary Fig. 1d), which confirm the over-coupling of the TM_{00} mode family in C-band with low extinction ratios (<1 dB). With the resonances identified and fitted, the experimental total quality factors (i.e., Q^{load}) for pump and signal are extracted and depicted in Fig. 2d, showing good agreement with the simulation. Q^{load} of the signal is 1.3×10^6, higher than that of the pump resonance (Q_p^{load}=2.8×10^5) near 191.4 THz, see Figs. 2c and 2d, which facilitates comb generation to be triggered and dominated by the signal.

The resonant frequencies f_μ and the four-wave mixing phase matching parameter,

$$\Delta f_\mu = f_\mu + f_{-\mu} - 2f_0,\ \mu = 0, \pm1, \pm2, \ldots, \qquad (1)$$

were computed numerically and plotted in Figs. 2e and 2f, coinciding with the experimental data (circles) very well. The signal and idler frequencies are determined from the condition of the parametric gain achieving its threshold value, which is most readily satisfied for a spread of modes in the proximity of the mode best complying with $\Delta f_\mu = 0$. Achieving $\Delta f_\mu = 0$ without invoking nonlinear frequency shifts is possible for large values of μ, when there is a change between anomalous and normal dispersion. A plot of the phase-matching parameter vs mode numbers, μ, for our resonator is shown in Fig. 2f, see also prior results in Refs. [21–28]. Defining dispersion as $D_{2\mu} = f_{\mu+1} + f_{\mu-1} - 2f_\mu$, we find that the groups of modes around the pump and signal have weakly anomalous dispersions, $D_{2p} = 1.7$MHz and $D_{2s} = 2.9$MHz, while the idler dispersion is large and normal, $D_{2i} = -22.7$MHz. The FSRs of the pump, signal, and idler are found to be $D_{1p} = 198.99$ GHz and $D_{1s} = 199.75$ GHz, and $D_{1i} = 200.73$ GHz, respectively.

The comb characterisation setup is schematically shown in Fig. 3a, where the amplified pump is coupled into the microresonator via a lensed fibre. For on-chip power of 250 mW, we observed the excitation of monochromatic signal and idler waves with the frequencies predicted by zeros of the phase-matching parameter, see Fig. 3b, broadly in agreement with prior work on Kerr OPOs [21–28]. We also tuned the signal and idler frequencies by tuning a range of various modes, see Supplementary Fig. 2. The output powers of the pump and signal in Fig. 3b are 17.4 dBm and 5.4 dBm, respectively, corresponding to an on-chip conversion efficiency of approximately 2%, which can be further improved by engineering the coupling rate and implementing temperature control. We note that since the signal is gaining energy from a product of the pump and idler amplitudes, with the latter being squared, the sufficiently high idler's Q is as critical as sufficiently high signal Q's for the generation of strong CW signals, see the Q versus mode number plot in Fig. 2d.

For on-chip pump powers ranging from 375 to 500 mW, we successfully observed hyperparametric soliton states corresponding to low-noise, three-colour frequency combs (see Figs. 3c-3g, 4, and 5), which we describe in detail below. The microresonator chip was mounted on a temperature-controlled copper stage to enable tuning of the phase-matching condition. Figure 3c presents comb power traces with the pump suppressed, as the pump wavelength was swept (0.5 nm/s) for six fixed on-chip pump power values. The green-shaded regions indicate soliton steps. A representative soliton spectrum (Fig. 3d) exhibits three triangular spectral bands centred at the idler, pump, and signal frequencies, with the signal band showing the highest comb power by a significant margin.

A pronounced feature of the soliton spectra is the dominance of the signal comb power over the pump and idler combs. Specifically, the total power of the pump comb accounts for only 4% of the signal comb power, excluding the central lines of both combs. Coherence of the soliton state was confirmed via heterodyne detection between the comb line at $\mu = -6$ and a reference tunable semiconductor laser (TSL), yielding a narrow beat note, see Fig. 3d. To measure the soliton repetition rate, f_{rep}, we employed an electro-optic (EO) comb generator [52], see Supplementary Fig. 3. The comparison between spectra with and without modulation is shown in Fig. 3e. A spectral region near 191.2 THz was filtered and used for radio-frequency (RF) detection, see Figs. 3f and 3g. With a frequency offset Δf of 419.5 MHz and a modulation frequency $f_{mod} = 25$ GHz, the

ARTICLE IN PRESS

repetition rate is $f_{rep} = 8 \times f_{mod} - \Delta f \approx 199.58$ GHz. This value closely matches the signal FSR in the linear regime, $D_{1s} = 199.75$ GHz, unambiguously indicating that the dominant signal pulse drives the repetition rate locking across the entire comb spectrum. By fitting the signal spectrum with a sech-squared function, we found that the soliton has a 3-dB bandwidth of 2 THz, giving a transform-limited pulse duration of 158 fs at full width half maximum.

The fact that the central signal mode at $\mu = 253$ dominates the comb spectrum generated around it should also be highlighted. This property contrasts sharply with that of parametric solitons in degenerate OPOs [32–34], which exhibit zero background and a central frequency that blends smoothly into the rest of the comb, cf. Figs. 1d and 1h. The strong central sideband in the signal comb in Fig. 3d should be compared with no such feature in the parametric soliton data in Fig. 2a(iv) in [32], Fig. 4d in [34], and Figs. 4a-4b in [33]. This effect is even more striking in the idler field at $\mu = -253$. Thus, we are dealing with multi-colour mode-locked pulses with a background shaped by the monochromatic parametrically generated signal and idler waves. This distinct behaviour motivates our use of the term hyperparametric soliton, as was already discussed in the previous section, see Fig. 1.

To test the tunability of hyperparametric solitons, we measured soliton generation across a range of resonators with varying geometries, each providing different phase-matching conditions. In particular, changing the ring width from 2530 to 2610 nm, while maintaining the pump at 191.1 THz, has led to a shift of the signal frequency by 2.3 THz, as shown in Supplementary Fig. 4a. We have further pumped a sequence of resonances in the interval from 191.4 THz to 193.6 THz and tuned the signal frequency from 242 THz to 249.7 THz, as shown in Fig. S4b. Correspondingly, the idler frequency was adjusted from 140.8 THz to 137.8 THz. The EDFA's range was the main factor limiting the observed tuning range.

Since no present concept or theory explains our measurements, it appears instructive to outline our numerical results and their interpretations. The first step in our analysis of mechanisms of the hyperparametric soliton generation was to solve the problem of three-wave parametric interaction of the $\mu = 0$ mode with several pairs of the signal and idler in the proximity of the $\Delta f_\mu = 0$ point, see Methods. Numerically computed signal components of all OPO states found above the parametric threshold for a chosen input power are shown in Fig. 4a. The pump, $\mu = 0$ mode, becomes strongly depleted by the generated signal and idler pairs so that its dependence on the laser frequency deviates from the parametric-process-free nonlinear resonance shown by the dashed line in Fig. 4b.

Notably, generating $|\mu| = 253$, 254, and 255 states leads to the bistable OPOs. One should note that the negative-detuning range of the 253 state stays isolated from the range of detunings where multiple other parametric states coexist, see Fig. 4a and Fig. 1f. We name the upper and lower branches of the bistability loop made by this state as OPO-1 and OPO-2. However, the instabilities of OPO-1 and OPO-2 relative to the excitation of other modes (modulational instability) can not be excluded.

To check stability and instability scenarios, we modelled a system of coupled equations for the amplitudes a_μ of the resonator modes $\mu = -512, \ldots, 0, \ldots, 511$, covering the spectrum from 90 to 290 THz, see Methods. We have found that the OPO-1 is typically modulationally unstable, whereas OPO-2 is typically stable over the detuning interval during which they coexist, a condition that leads to the generation of hyperparametric solitons. The spectral carpet shown in Fig. 4d represents a bifurcation diagram computed by varying the laser frequency from large negative detunings, $\delta = (f_0 - f_p)/\frac{1}{2}\kappa_0$, to positive ones, illustrating the modulational instability and soliton generation processes. Here, f_p is the laser frequency and κ_0 is the width of the pumped resonance. CW parametric generation begins at $\delta \approx -2.16$ and destabilises due to sideband generation at $\delta \approx -1.6$, forming three-colour frequency combs. These then evolve into hyperparametric solitons that exist for δ values in the $(-0.65, -0.06)$ range.

A numerically computed spectrum of the hyperparametric soliton (see Fig. 4c) qualitatively matches the typical experimentally observed spectra in Fig. 3d. The reconstructed pulse envelope profiles for a hyperparametric soliton's signal, pump, and idler components are shown in Fig. 4e. It shows that the pump and idler waves are quasi-CW fields, and only the signal is a pronounced bright soliton resting on a background with finite amplitude.

The idler is not expected to make a pulse because its frequency lies in the interval of large normal dispersion. While the pump is in the anomalous dispersion range, it experiences a loss rate three times higher than the signal and also remains quasi-CW. For the pump to trigger soliton generation of its own, i.e., without the parametric process involved, requires the laser frequency to be tuned closer to the tip of its resonance ($\delta \approx 4$ on the dashed black line in Fig. 4b).

When spectra of the pump, signal, and idler combs remain well isolated from each other, one can split the full coupled-mode system into equations for three modal groups and introduce the respective envelope functions, A_p, A_s, and A_i, Fig. 4 caption and Methods. By checking the signal equation, see Eq. (9) in Methods, reveals that the signal soliton centred on a mode μ' is excited by the quasi-CW nonlinear polarisation wave induced by the four-wave mixing process $A_p^2 A_i^* \approx a_0^2 a_{-\mu'}^*$.

Thus, the signal equation can be considered the generalised Lugiato-Lefever equation, where the pump has a complex dependence on the detuning introduced by the parametric process. The latter is anticipated to be the

ARTICLE IN PRESS

OPO-2 state. Diamonds, squares, and crosses in Fig. 4e show perfect matching between the hyperparametric soliton tails and the power values of the signal, pump and idler of the OPO-2 state, see Fig. 4a. This finding unambiguously confirms that the hyperparametric soliton has the background wave matching the OPO-2 state.

By pumping different resonator modes, tuning pump power, and varying the phase matching parameter, we have further checked that conditions for the hyperparametric solitons to exist are that the first parametric state bifurcating from the pump for the negative detunings must become bistable and provide a range of parameters (pump power and detuning) where the lower (OPO-2) branch is stable and the upper (OPO-1) branch is modulationally unstable. These conditions are typically met when the net signal losses are sufficiently small and the power of the four-wave mixing term, $a_0^2 a^*_{-\mu'}$, driving the signal mode $a_{\mu'}$, is sufficiently high.

For the soliton generation, we recorded a video (see Supplementary Video 1) showing how the signal and pump spectra evolve during manual frequency tuning across the hyperparametric soliton range. Initially, non-solitonic combs replace the monochromatic signal and pump, which then evolve into soliton generation. The strong, $\approx$ 8dBm, central sideband in the signal component rising above the comb starting around -8 dBm, unambiguously points to the hyperparametric regime. The soliton existence on the negatively detuned tail of the resonance, where intraresonator fields and thermal effects are modest, enables the simplicity of the manual tuning. Tuning to the range of positive detunings boosts the circulating power, leading to the sudden loss of resonance due to thermal shifts. Experimental access to these regimes may be the subject of future work using one of the established techniques for observing positively detuned non-parametric solitons of the Lugiato-Lefever equation [4, 51].

We also observed the generation of spectrally broad signals and idler combs at relatively high pump powers, see Supplementary Fig. 5. For large detuning, a sparse Turing-pattern-like OPO comb has a line separation of 11 FSR, which then gradually transitions to combs with broader, densely filled spectra. The pump-only Turing-pattern-like comb with the 28 FSR line-to-line separation is seen at the end of this experimental sequence. This level of pump power already takes us outside the hyperparametric soliton range, while pure Kerr solitons can be found numerically at these powers for red detuning. They are, however, not observed experimentally due to the lack of measures to control thermal effects in our setup.

The measured spectra can vary from a single soliton to quasi-crystals or soliton crystals by slightly changing the pump power, as shown in Fig. 5a. In crystals containing N solitons, only every Nth mode is excited, while quasi-crystals exhibit weaker lines between the strong spectral peaks. With the same resonator, we successfully excited the soliton crystals with N=2, 3, 4, 5, 6, 7. Additionally, multi-soliton non-crystal states, where N pulses are situated far apart from the $2\pi/N$ separation distances, have also been frequently observed, see the two-soliton in state (ii). A single beat note near 1.5 GHz in heterodyne measurements shown in Fig. 5b confirms that the two-, three-, and four-soliton states are completely coherent. However, the five-, six-, and seven-soliton crystals are typically the breather states [53, 54].

Experimentally, we have observed the OPO comb spectra with signal and idler tuned between 230 and 249THz (1.3–1.2μm) and $138-150$THz ($2.2-2\mu$m), respectively. At the extremities of this range, a broadband OPO comb was generated but not a soliton state due to the unoptimized coupling rate. While dispersion engineering allows extremely broad-band phase matching [23], the existence of multi-colour solitons imposes its own constraints on the balance of dispersion and quality factors for which a complete understanding should be the subject of future work.

As the number of hyperparametric solitons in a crystal increases, the magnitude of the central sidebands in the idler and pump fields remains dominant. Conversely, the sidebands in the signal field decrease significantly. This is because the signal background rapidly loses power as the ring gets filled with pulses. Meanwhile, the pump and idler fields remain quasi-cw, with their power being only weakly dependent on the number of solitons in the crystal. This behavious has been observed in the experimental and numerical data, see Figs. 5a,b and 5c,d.

Soliton crystals have now emerged as a sub-field that connects photonics, condensed matter, and topological physics [55–60], while the multi-soliton and crystal studies included parametric systems [38, 61], the hyperparametric frequency conversion effect paves a new path for their investigation.

DISCUSSION

We demonstrated hyperparametric three-colour idler-pump-signal solitons in a nondegenerate Kerr microresonator OPO with a 200 GHz pulse repetition rate. The idler and pump soliton components exhibit quasi-CW behaviour, while the signal component forms a pronounced bright soliton pulse sitting on a parametrically generated background. This soliton regime arises when one of the above-threshold signal-idler pairs makes a hysteresis loop (bistability) from the modulationally unstable high-power and stable low-power OPO states. Our modelling shows that this OPO bistability occurs at negative pump detunings, which avoids the positive detuning region typically associated with pump-centered Lugiato–Lefever solitons. At negative detunings, intra-resonator powers remain relatively low, minimizing unwanted thermal ef-

ARTICLE IN PRESS

ARTICLE IN PRESS

fects. The quasi-CW nature of the pump and idler components is maintained through a combination of strong coupling losses at the pump (overcoupled resonator) and normal dispersion at the idler wavelength.

Nondegenerate OPOs provide broad and flexible tunability through resonator geometry and temperature control of the refractive index and phase-matching conditions [21–28]. This contrasts with degenerate OPOs, in which the signal frequency is strictly determined by the pump [32–34]. We also observed and reported the formation of crystals and breather states of hyperparametric solitons. Specifically, we generated solitons in the optical communication O-band using a C-band pump source. Expanding the availability of O-band light sources based on silicon photonics is a key milestone in the ongoing development of low-power optical interconnects for data center applications [62].

Overall, our results on hyperparametric solitons open new avenues for studying their dynamics and interaction with other soliton types in nondegenerate Kerr and especially in $\chi^{(2)}$ microresonators, where realising comb generation around widely separated and tunable signal and idler frequencies remains an open challenge.

METHODS

Device fabrication and characterisation. The Si_3N_4 microresonators were fabricated using a deep ultraviolet (DUV) based subtractive process on 4-inch silicon wafers. A 4 μm thermal oxide layer was first grown as the bottom cladding. To mitigate the high tensile stress in thick Si_3N_4 films, interconnected stress-release trenches (3.5 μm depth) were patterned in the SiO_2 substrate using dry etching, spaced 10-30 μm from waveguide regions to ensure waveguide uniformity. A 770 nm thick stoichiometric Si_3N_4 layer was then deposited in a single low-pressure chemical vapour deposition (LPCVD) step, achieving 0.6% thickness uniformity across the wafer. Waveguides were patterned using KrF 248 nm DUV stepper lithography with 180 nm resolution, followed by anisotropic dry etching with a C_xF_y chemistry. An LPCVD SiO_2 hard mask was employed during etching to achieve smooth sidewalls with 87° sidewall angles. The devices underwent high-temperature annealing at 1200°C for 11 hours in N_2 atmosphere to reduce hydrogen-related absorption losses. A 1.3 μm thick LPCVD SiO_2 top cladding was then deposited and subjected to identical annealing conditions.

OFC measurements. To characterize the resonator's transmission, we swept two separate tunable lasers across the 1480–1640 nm, and 1260-1360 nm wavelength ranges with a high resolution of 0.1 pm and recorded the output optical power. These transmission spectra enabled the extraction of key resonator parameters, including resonance linewidths, free spectral ranges (FSRs), and phase-matching conditions. For hyperparametric soliton generation, we used a C-band tunable laser source, amplified by an erbium-doped fiber amplifier (EDFA), which was coupled into the waveguide through a lensed fiber. Before the lensed fiber, a fiber polarization controller (FPC) was employed to optimize the pump polarization, and a bandpass filter (BPF) was inserted to suppress amplified spontaneous emission (ASE) noise.

The output light was collected using a second lensed fiber and split into two detection paths. One path, carrying the majority of the signal, was directed to optical spectrum analyzers (OSAs) for spectral monitoring. Simultaneously, the other path was routed either through a fiber Bragg grating (FBG) for comb power monitoring using a digital storage oscilloscope (DSO), or through a bandpass filter (BPF) and combined with an auxiliary tunable semiconductor laser (TSL) for radio-frequency (RF) noise analysis using an electrical spectrum analyzer (ESA). Access to optical parametric oscillation (OPO) sidebands and hyperparametric soliton states was achieved by gradually tuning the pump laser into resonance, either through continuous wavelength sweeping or manual adjustment. The characteristic soliton dynamics are illustrated in the Supplementary Video 1, which captures the manual tuning of the pump wavelength from 1566.37 nm to 1566.42 nm at an on-chip pump power of 425 mW.

Nonlinear modelling. Multimode intra-resonator field is expressed as

$$\mathcal{A}e^{iM\vartheta - i\omega_p \tilde{t}} + c.c., \ \mathcal{A} = \sum_{\mu} a_\mu(\tilde{t}) e^{i\mu\vartheta}. \tag{2}$$

Here, $\vartheta = (0, 2\pi]$ is the angular coordinate in the laboratory frame, $\tilde{t}$ is time and a_μ are mode amplitudes and $\mu = 0, \pm 1, \pm 2, \ldots$ is the relative mode number. Coupled-mode equations governing nonlinear interactions between a_μ are [63–66]

$$\begin{aligned} i\partial_t a_\mu = &-\gamma \sum_{\mu_1\mu_2\mu_3} \widehat{\delta}_{\mu,\mu_1+\mu_2-\mu_3} a_{\mu_1} a_{\mu_2} a^*_{\mu_3} \\ &+ (f_\mu - f_p) a_\mu - \frac{\kappa_\mu}{2}\big(a_\mu - \widehat{\delta}_{\mu,0}\sqrt{b\mathcal{W}}\big). \end{aligned} \tag{3}$$

Here, $\widehat{\delta}_{\mu,\mu'} = 1$ for $\mu = \mu'$ and is zero otherwise. The resonator spectrum, $f_\mu = \omega_\mu/2\pi$, and the mode number dependent linewidth, κ_μ, were computed using Lumerical software, see Fig. 2. Since we work with frequencies, f_μ, and not the angular frequencies, ω_μ, time t in Eq. (3) was redefined as $t = 2\pi\tilde{t}$. The pump laser frequency, f_p, is tuned around $f_0 = 191.44$THz corresponding to the $M = 820$ resonance. $\mathcal{W}$ is the on-chip laser power, $b = 179.5$ is the resonator power build-up factor for $f_p = f_0$. $\gamma = f_0 n_2/S n_0$ is the nonlinear parameter [16]; $n_2 = 2.6 \cdot 10^{-19}\mathrm{m}^2/\mathrm{W}$ (Kerr coefficient), $S = 1.32 \cdot 10^{-12}\mathrm{m}^2$ (mode area), $n_0 = 2.022$ (refractive index), $\gamma = 18.65$MHz/W. $|a_\mu|^2$ represents intraresonator powers of the comb lines scaled to have units of

ARTICLE IN PRESS

Watts [66]. Data shown in Figs. 3c-e, 4 are obtained by modelling Eq. (3). While numerically solving Eq. (3), we divided them by $\kappa_0/2$, $\kappa_0 = 683$MHz. The scaling parameter applied to plot dimensionless modal powers in Figs. 4a,b,e is $\kappa_0/2\gamma = 18.3$W. Linewidth parameters are $\kappa_\mu = f_\mu/Q_\mu^{\rm load}$, see Fig. 2d and Supplementary Table I.

Three-wave OPO states, represented by the pump mode and a signal-idler pair, see Figs. 4a,b, were computed from the three-mode reduction of Eq. (3).

$$\begin{aligned} i\partial_t a_0 &= -2\gamma a_\mu a_{-\mu} a_0^* - \gamma(|a_0|^2 + 2|a_\mu|^2 + 2|a_{-\mu}|^2)a_0 \\ &\quad + (f_0 - f_p)a_0 - i\frac{\kappa_0}{2}(a_0 - \sqrt{b\mathcal{W}}), \\ i\partial_t a_\mu &= -\gamma a_0^2 a_{-\mu}^* - \gamma(|a_\mu|^2 + 2|a_0|^2 + 2|a_{-\mu}|^2)a_\mu \\ &\quad + (f_\mu - f_p)a_\mu - i\frac{\kappa_\mu}{2}a_\mu, \\ i\partial_t a_{-\mu} &= -\gamma a_0^2 a_\mu^* - \gamma(|a_{-\mu}|^2 + 2|a_0|^2 + 2|a_\mu|^2)a_{-\mu} \\ &\quad + (f_{-\mu} - f_p)a_{-\mu} - i\frac{\kappa_{-\mu}}{2}a_{-\mu}. \end{aligned} \tag{4}$$

Parametric terms are placed first after the equal signs in all three equations. The role of phase-matching parameter, Δf_μ, see Eq. (1), in the three-wave model becomes explicit on the observation that

$$f_{\pm\mu} - f_p = \frac{1}{2}\Delta f_\mu + (f_0 - f_p) \pm \zeta_\mu, \tag{5}$$

while the $\zeta_\mu = (f_\mu - f_{-\mu})/2$ term can be eliminated from Eq. (4) by substituting $a_{\pm\mu} = \tilde{a}_{\pm\mu}\exp(\mp i\zeta_\mu t)$. So that, Eq. (4) becomes

$$\begin{aligned} i\partial_t a_0 &= -2\gamma \tilde{a}_\mu \tilde{a}_{-\mu} a_0^* - \gamma(|a_0|^2 + 2|\tilde{a}_\mu|^2 + 2|\tilde{a}_{-\mu}|^2)a_0 \\ &\quad + (f_0 - f_p)a_0 - i\frac{\kappa_0}{2}(a_0 - \sqrt{b\mathcal{W}}), \\ i\partial_t \tilde{a}_\mu &= -\gamma a_0^2 \tilde{a}_{-\mu}^* - \gamma(|\tilde{a}_\mu|^2 + 2|a_0|^2 + 2|\tilde{a}_{-\mu}|^2)\tilde{a}_\mu \\ &\quad + (\tfrac{1}{2}\Delta f_\mu + f_0 - f_p)a_\mu - i\frac{\kappa_\mu}{2}\tilde{a}_\mu, \\ i\partial_t \tilde{a}_{-\mu} &= -\gamma a_0^2 \tilde{a}_\mu^* - \gamma(|\tilde{a}_{-\mu}|^2 + 2|a_0|^2 + 2|\tilde{a}_\mu|^2)\tilde{a}_{-\mu} \\ &\quad + (\tfrac{1}{2}\Delta f_\mu + f_0 - f_p)\tilde{a}_{-\mu} - i\frac{\kappa_{-\mu}}{2}\tilde{a}_{-\mu}. \end{aligned} \tag{6}$$

Equation (6) explicitly shows that the OPO operation depends on the pump detuning, $f_0 - f_p$, and the phase-mismatch parameter, Δf_μ.

Values of the relative linewidth parameters for the relevant signal-idler pairs are specified in Supplementary Table I. Uncertainties in the parameter selection for numerical modelling come from the absence of experimental data on the loss values in the proximity of the signal and idler fields and temperature-induced fluctuations of the refractive index impacting phase-matching conditions.

Pulse envelopes, A_p, A_s and A_i, corresponding to the well-separated pump, signal and idler spectra can be reconstructed from the modal amplitudes as

$$\begin{aligned} A_p &= \sum\nolimits_{\mu=-N}^{N} a_\mu e^{i\mu\theta}, \\ A_s &= e^{-i\zeta_{\mu_0}t}\tilde{A}_s,\ \tilde{A}_s = \sum\nolimits_{\mu=\mu_0-N}^{\mu_0+N} \tilde{a}_\mu e^{i\mu\theta}, \\ A_i &= e^{i\zeta_{\mu_0}t}\tilde{A}_i,\ \tilde{A}_i = \sum\nolimits_{\mu=-\mu_0-N}^{-\mu_0+N} \tilde{a}_\mu e^{i\mu\theta}, \end{aligned} \tag{7}$$

where μ_0 and N can be chosen, e.g., as $\mu_0 = 253$ and $N = 100$. We have now replaced the angular variable ϑ with $\theta = \vartheta - D_{1s}t$ rotating with repetition rate at the signal frequency and will approximate dispersions only upto the second-order terms. Equations for three envelopes, although their use for modelling comb dynamics is left for future work, allow for an understanding of the hyperparametric soliton generation at a qualitative level and contrast it with the previously reported parametric solitons [32–34]:

$$\begin{aligned} i\partial_t A_p &= -i(D_{1p} - D_{1s})\partial_\theta A_p - \frac{1}{2}D_{2p}\partial_\theta^2 A_p - 2\gamma\tilde{A}_s\tilde{A}_i A_p^* \\ &\quad + (\Delta_p - \gamma|A_p|^2)A_p - i\frac{\kappa_0}{2}(A_p - \sqrt{b\mathcal{W}}), \end{aligned} \tag{8}$$

$$\begin{aligned} i\partial_t \tilde{A}_s &= -\frac{1}{2}D_{2s}\partial_\theta^2\tilde{A}_s - \gamma A_p^2\tilde{A}_i^* \\ &\quad + (\Delta_s - \gamma|\tilde{A}_s|^2)\tilde{A}_s - i\frac{\kappa_{\mu_0}}{2}\tilde{A}_s, \end{aligned} \tag{9}$$

$$\begin{aligned} i\partial_t \tilde{A}_i &= -i(D_{1i} - D_{1s})\partial_\theta\tilde{A}_i - \frac{1}{2}D_{2i}\partial_\theta^2\tilde{A}_i - \gamma A_p^2\tilde{A}_s^* \\ &\quad + (\Delta_i - \gamma|\tilde{A}_i|^2)\tilde{A}_i - i\frac{\kappa_{-\mu_0}}{2}\tilde{A}_i, \end{aligned} \tag{10}$$

where we omitted higher-order dispersion, and introduced short-hand notations for effective detunings incorporating pump detuning, phase-mismatch, and nonlinear cross-phase modulation terms,

$$\Delta_p = f_0 - f_p - 2\gamma(|\tilde{A}_s|^2 + |\tilde{A}_i|^2), \tag{11}$$

$$\Delta_s = \tfrac{1}{2}\Delta f_{\mu_0} + f_0 - f_p - 2\gamma(|A_p|^2 + |\tilde{A}_i|^2), \tag{12}$$

$$\Delta_i = \tfrac{1}{2}\Delta f_{\mu_0} + f_0 - f_p - 2\gamma(|A_p|^2 + |\tilde{A}_s|^2). \tag{13}$$

Since, in the hyperparametric soliton regime, the pump and idler fields are quasi-CW, the Δ_s parameter can be approximately treated as a quasi-constant, $\partial_\theta\Delta_s \approx 0$, and equations for $A_p(t,\theta)$ and $\tilde{A}_i(t,\theta)$ can be approximated by equations for $a_0(t)$ and $\tilde{a}_{-\mu_0}(t)$. Then, Eq. (9) takes the form of the generalised Lugiato-Lefever model, where the four-wave mixing term, $A_p^2\tilde{A}_i^* \approx a_0^2\tilde{a}_{-\mu_0}^*$, $\partial_\theta(A_p^2\tilde{A}_i^*) \approx 0$, plays the role of an effective pump, implicitly parametrised by the actual pump detuning, $f_0 - f_p$, and power, $\mathcal{W}$. It is important to note that, even in this approximation, the effective pump in the signal equation, Eq. (9), is not an independent parameter like the pump term in the LLE model [4]. Instead, it is a variable whose stationary values and evolution are determined by the pump, $a_0(t)$, and idler amplitudes, $\tilde{a}_{-\mu_0}(t)$, which satisfy additional equations. The normalised repetition rate

ARTICLE IN PRESS

ARTICLE IN PRESS

differences and dispersion values are $(D_{1p} - D_{1s})/\frac{1}{2}\kappa_0 = -2.2126$, $(D_{1i} - D_{1s})/\frac{1}{2}\kappa_0 = 2.8199$, $D_{2p}/\frac{1}{2}\kappa_0 = 0.0052$, $D_{2s}/\frac{1}{2}\kappa_0 = 0.0085$ and $D_{2i}/\frac{1}{2}\kappa_0 = -0.0699$.

Eqs. (8)-(10) are transformed to the equations for the degenerate Kerr OPO used in Ref. [33] to demonstrate parametric solitons, when A_p is replaced with A_s, while $\tilde{A}_s$ and $\tilde{A}_i$ become two pump fields A_{p1} and A_{p2}, so that the external pump term, $\sqrt{b\mathcal{W}}$, is moved from Eq. (8) to Eqs. (9), (10). A_{p1} and A_{p2} can be approximated as quasi-CW fields [33], $\partial_\theta(A_{p1}A_{p2}) \approx 0$, so that Eq. (8) becomes a parametric Ginzburg-Landau equation,

$$\begin{aligned} i\partial_t A_s &= -\frac{1}{2}D_{2s}\partial_\theta^2 A_s - 2\gamma A_{p1}A_{p2}A_s^* \\ &+(\Delta_s - \gamma|A_s|^2 - i\frac{\kappa_0}{2})A_s, \end{aligned} \tag{14}$$

possessing explicit bright soliton solutions on zero background [33–36, 39–41].

Data availability

The raw data comprise high-volume measurements that require specialist processing and are not deposited in a public repository but can be made available from the corresponding authors upon request.

REFERENCES

[1] A. Pasquazi, et al. Micro-combs: A novel generation of optical sources, Physics Reports **729**, 1 (2018).

[2] S.A. Diddams, K. Vahala, and T. Udem, Optical frequency combs: Coherently uniting the electromagnetic spectrum, Science **369**, eaay3676 (2020).

[3] L. Chang, S.T. Liu, and J.E. Bowers, Integrated optical frequency comb technologies, Nature Photonics **16**, 95 (2022).

[4] T. J. Kippenberg, A. L. Gaeta, M. Lipson, and M.L. Gorodetsky, Dissipative Kerr solitons in optical microresonators, Science **361**, 567 (2018).

[5] Q. Li, et al. "Stably accessing octave-spanning microresonator frequency combs in the soliton regime," Optica **4**, 193–203 (2017).

[6] M.H.P. Pfeiffer, et al. "Octave-spanning dissipative Kerr soliton frequency combs in Si3N4 microresonators," Optica **4**, 684 (2017).

[7] Y. Song, Y. Hu, X. Zhu, K. Yang, and M. Lončar, Octave-spanning Kerr soliton frequency combs in dispersion- and dissipation-engineered lithium niobate microresonators, Light: Science & Applications **13**, 225 (2024).

[8] S. Zhang, J. M. Silver, T. Bi, and P. Del'Haye, Spectral extension and synchronization of microcombs in a single microresonator, Nature Communications **11**, 6384 (2020).

[9] G. Moille, E. F. Perez, J. R. Stone, A. Rao, X. Lu, T. S. Rahman, Y. K. Chembo, and K. Srinivasan, Ultra-broadband Kerr microcomb through soliton spectral translation, Nature Communications **12**, 7275 (2021).

[10] Moille, G., Shandilya, P., Niang, A. et al. Versatile optical frequency division with Kerr-induced synchronization at tunable microcomb synthetic dispersive waves. Nat. Photon. **19**, 36 (2025).

[11] S. Zhang, T. Bi, G. N. Ghalanos, N. P. Moroney, L. Del Bino, and P. Del'Haye, Dark-bright soliton bound states in a microresonator, Physical Review Letters **128**, 033901 (2022).

[12] Yu, S. P., Lucas, E., Zang, J. & Papp, S. B. A continuum of bright and dark-pulse states in a photonic-crystal resonator. Nat. Commun. **13**, 3134 (2022).

[13] Q.-F. Yang, X. Yi, K. Y. Yang, and K. Vahala, Stokes solitons in optical microcavities, Nature Physics 13, 53 (2017).

[14] T. Tan, Z. Yuan, H. Zhang, G. Yan, S. Zhou, N. An, B. Peng, G. Soavi, Y. Rao, and B. Yao, Multispecies and individual gas molecule detection using stokes solitons in a graphene over-modal microresonator, Nature communications **12**, 6716 (2021).

[15] C.R. Menyuk, P. Shandilya, L. Courtright, G. Moille, and K. Srinivasan, "Multi-color solitons and frequency combs in microresonators," Opt. Express **33**, 21824 (2025).

[16] Y. He, et al. "Self-starting bi-chromatic LiNbO3 soliton microcomb," Optica **6**, 1138 (2019).

[17] Lu, J., Puzyrev, D.N., Pankratov, V.V. et al. Two-colour dissipative solitons and breathers in microresonator second-harmonic generation. Nat Commun **14**, 2798 (2023).

[18] Kippenberg, T.J., Spillane, S.M., and Vahala, K.J. Kerr-nonlinearity optical parametric oscillation in an ultrahigh-Q toroid microcavity. Phys. Rev. Lett. **93**, 083904 (2004).

[19] J.S. Levy, A. Gondarenko, M.A. Foster, A.C. Turner-Foster, A.L. Gaeta, and M. Lipson, CMOS-compatible multiple-wavelength oscillator for on-chip optical interconnects, Nature Photonics **4**, 37 (2010).

[20] L. Razzari, D. Duchesne, M. Ferrera, R. Morandotti, S. Chu, B.E. Little, and D.J. Moss, CMOS-compatible integrated optical hyper-parametric oscillator, Nature Photonics **4**, 41 (2010).

[21] N. L. B. Sayson, T. Bi, V. Ng, H. Pham, L. S. Trainor, H. G. Schwefel, S. Coen, M. Erkintalo, and S. G. Murdoch, Octave-spanning tunable parametric oscillation in crystalline kerr microresonators, Nature Photonics **13**, 701 (2019).

[22] S. Fujii, S. Tanaka, M. Fuchida, H. Amano, Y. Hayama, R. Suzuki, Y. Kakinuma, and T. Tanabe, Octavewide phase-matched four-wave mixing in dispersion engineered crystalline microresonators, Optics letters **44**, 3146 (2019).

[23] E. F. Perez, G. Moille, X. Lu, J. Stone, F. Zhou, and K. Srinivasan, High-performance Kerr microresonator optical parametric oscillator on a silicon chip, Nature Communications **14**, 242 (2023).

[24] D. Pidgayko, A. Tusnin, J. Riemensberger, A. Stroganov, A. Tikan, and T.J. Kippenberg, Voltage-tunable optical parametric oscillator with an alternating dispersion dimer integrated on a chip, Optica **10**, 1582 (2023).

[25] X. Lu, G. Moille, A. Singh, Q. Li, D. A. Westly, A. Rao, Su-Peng Yu, T. C. Briles, S.B. Papp, and K. Srinivasan, "Milliwatt-threshold visible–telecom optical parametric oscillation using silicon nanophotonics," Optica **6**, 1535 (2019).

[26] Y. Tang, Z. Gong, X. Liu, and H. X. Tang, Widely sepa-

ARTICLE IN PRESS

ARTICLE IN PRESS

rated optical Kerr parametric oscillation in AlN microrings, Optics Letters **45**, 1124 (2020).

[27] Y. Zhao, J. K. Jang, X. Ji, Y. Okawachi, M. Lipson, and A. L. Gaeta, "Large regenerative parametric amplification on chip at ultra-low pump powers," Optica **10**, 819 (2023).

[28] P. Zhao, V. Shekhawat, M. Girardi, Z. He, V. Torres-Company, and P. A. Andrekson, Ultra-broadband optical amplification using nonlinear integrated waveguides, Nature **640**, 918 (2025).

[29] Y. Okawachi, M. Yu, J. K. Jang, X. Ji, Y. Zhao, B. Y. Kim, M. Lipson, and A. L. Gaeta, "Demonstration of chip-based coupled degenerate optical parametric oscillators for realizing a nanophotonic spin-glass," Nat. Commun. **11**, 4119 (2020).

[30] L. Ledezma, A. Roy, L. Costa, R. Sekine, R. Gray, Q. Guo, R. Nehra, R. M. Briggs, and A. Marandi, "Octave-spanning tunable infrared parametric oscillators in nanophotonics," Sci. Adv. **9**, eadf9711 (2023).

[31] A.Y. Hwang, H.S. Stokowski, T. Park, M. Jankowski, T.P. McKenna, C. Langrock, J. Mishra, V. Ansari, M.M. Fejer, and A.H. Safavi-Naeini, "Mid-infrared spectroscopy with a broadly tunable thin-film lithium niobate optical parametric oscillator," Optica **10**, 1535 (2023).

[32] A. W. Bruch, X. Liu, Z. Gong, J. B. Surya, M. Li, C.-L. Zou, and H. X. Tang, Pockels soliton microcomb, Nature Photonics **15**, 21 (2021).

[33] G. Moille, M. Leonhardt, D. Paligora, N. Englebert, F. Leo, J. Fatome, K. Srinivasan, and M. Erkintalo, Parametrically driven pure-Kerr temporal solitons in a chip-integrated microcavity, Nature Photonics **18**, 617 (2024).

[34] N. Englebert, F. De Lucia, P. Parra-Rivas, C. M. Arab´ı, P.-J. Sazio, S.-P. Gorza, and F. Leo, Parametrically driven kerr cavity solitons, Nature Photonics **15**, 857 (2021).

[35] S. Longhi, "Localized structures in optical parametric oscillation," Phys. Scripta **56**, 611 (1997).

[36] K. Staliunas and V. J. Sanchez-Morcillo, "Localized structures in degenerate optical parametric oscillators," Opt. Commun. **139**, 306 (1997).

[37] S. Trillo and M.Haelterman, "Excitation and bistability of self-trapped signal beams in optical parametric oscillators," Opt. Lett. **23**, 1514 (1998).

[38] D.V. Skryabin and W. J. Firth, "Interaction of cavity solitons in degenerate optical parametric oscillators," Opt. Lett. **24**, 1056 (1999).

[39] J. W. Miles, Parametrically excited solitary waves, J. Fluid Mech. **148**, 451 (1984).

[40] S. Fauve and O. Thual, Solitary waves generated by subcritical instabilities in dissipative systems, Phys. Rev. Lett. **64**, 282 (1990).

[41] I. V. Barashenkov, M. M. Bogdan and V. I. Korobov, Stability Diagram of the Phase-Locked Solitons in the Parametrically Driven, Damped Nonlinear Schrödinger Equation, Europhysics Letters **15**, 113 (1991).

[42] D.V. Skryabin, A.R. Champneys, and W.J. Firth, Frequency Selection by Soliton Excitation in Nondegenerate Intracavity Down-conversion, Phys. Rev. Lett. **84**, 463 (2000).

[43] G.J. de Valcárcel, E. Roldán, and K. Staliunas, Cavity solitons in nondegenerate optical parametric oscillation, Optics Communications **181**, 207 (2000).

[44] A. B. Matsko, Hyperparametric frequency noise eater, Physical Review A **99**, 023843 (2019).

[45] J.R. Stone, G. Moille, X. Lu, and K. Srinivasan, Conversion Efficiency in Kerr-Microresonator Optical Parametric Oscillators: From Three Modes to Many Modes, Phys. Rev. Applied **17**, 024038 (2022).

[46] J. Yang, S.W. Huang, Z. Xie, M. Yu, D.L. Kwong, and C.W. Wong, Coherent satellites in multispectral regenerative frequency microcombs Communications Physics volume **3**, 27 (2020).

[47] Xinru Ji, Rui Ning Wang, Yang Liu, Johann Riemensberger, Zheru Qiu, and Tobias J. Kippenberg, "Efficient mass manufacturing of high-density, ultra-low-loss Si3N4 photonic integrated circuits," Optica **11**, 1397 (2024).

[48] G. Moille, Q. Li, T. C. Briles, S.-P. Yu, T. Drake, X. Lu, A. Rao, D. Westly, S. B. Papp, and K. Srinivasan, Broadband resonator-waveguide coupling for efficient extraction of octave-spanning microcombs, Optics Letters **44**, 4737 (2019).

[49] A. B. Matsko, A. A. Savchenkov, S.-W. Huang, and L. Maleki, Clustered frequency comb, Optics Letters **41**, 5102 (2016).

[50] N. L. B. Sayson, H. Pham, K. E. Webb, V. Ng, L. S. Trainor, H. G. Schwefel, S. Coen, M. Erkintalo, and S. G. Murdoch, Origins of clustered frequency combs in kerr microresonators, Optics Letters **43**, 4180 (2018).

[51] S. Zhang, et al. Sub-milliwatt-level microresonator solitons with extended access range using an auxiliary laser, Optica **6**, 206 (2019).

[52] J. Wang, Q. Wang, M. Xu, Y. Zhu, Y. Wang, H. Deng, and X. Cai, Highly tunable flat-top thin-film lithium niobate electro-optic frequency comb generator with 148 comb lines, Optics Express **33**, 23431 (2025).

[53] Yu, M., Jang, J., Okawachi, Y. et al. Breather soliton dynamics in microresonators. Nat Commun **8**, 14569 (2017).

[54] Afridi, A.A., et al. Breather solitons in AlN microresonators. Opt. Continuum **1**, 42 (2022).

[55] Cole, D.C., Lamb, E.S., Del'Haye, P. et al. Soliton crystals in Kerr resonators. Nature Photon **11**, 671 (2017).

[56] Karpov, M., Pfeiffer, M.H.P., Guo, H. et al. Dynamics of soliton crystals in optical microresonators. Nat. Phys. 15, 1071 (2019).

[57] Fan, Z., Puzyrev, D.N., Skryabin, D.V. Topological soliton metacrystals. Commun Phys **5**, 248 (2022).

[58] N. Englebert, R.M. Gray, L. Ledezma, and A. Marandi, "Topological Soliton Formation in a Nanophotonic Optical Parametric Oscillator," in CLEO 2024, Technical Digest Series (Optica Publishing Group, 2024), paper FW4M.6.

[59] Mittal, S., Moille, G., Srinivasan, K. et al. Topological frequency combs and nested temporal solitons. Nat. Phys. **17**, 1169 (2021).

[60] Christopher J. Flower et al, Observation of topological frequency combs, Science **384**, 1356 (2024).

[61] Y. Sun, C. Dupont, E.K. Akakpo, F. De Lucia, G. Semaan, S.P. Gorza, and F. Leo, Parametrically driven Kerr temporal soliton crystals. https://arxiv.org/abs/2504.04788 (2025).

[62] Malik, A. et al. Widely tunable, heterogeneously integrated quantum-dot O-band lasers on silicon, Photon. Res. **8**, 1551 (2020).

[63] Chembo, Y.K. & Yu, N. Modal expansion approach to optical-frequency-comb generation with monolithic whispering-gallery-mode resonators. Phys. Rev. A **82**, 033801 (2010).

ARTICLE IN PRESS

ARTICLE IN PRESS

[64] Herr, T. et al. Temporal solitons in optical microresonators. Nat. Photonics **8**, 145 (2014).
[65] Guo, X. et al. Efficient Generation of a Near-visible Frequency Comb via Cherenkov-like Radiation from a Kerr Microcomb, Phys. Rev. Appl. **10**, 014012 (2018).
[66] Skryabin, D.V. Hierarchy of coupled mode and envelope models for bi-directional microresonators with Kerr nonlinearity. OSA Continuum **3**, 1364 (2020).

Acknowledgements
This work was supported by a joint project between Research Ireland (SFI Grant No. 23/EPSRC/3920) and the UK Engineering and Physical Sciences Research Council (EPSRC Grant No. EP/X040844/1). Other support was received from CONNECT Centre (Grant No. 13/RC/2077.P2), the Royal Society (Grant No. IES/R3/223225), and Leading Innovation and Entrepreneurship Teams of Zhejiang (Grant No. 2023R01011).

Author contributions
H.W. performed the device design and measurements with the assistance from M.A., E.H.K., L.W., V.K., Q.W. and W.G.. X.J. and T.J.K. fabricated the microresonators. D.V.S. developed theory and performed numerical simulations of OPO operation and solitons. H.W., J.F.D., and D.V.S wrote the manuscript text. D.V.S. and J.F.D conceptualised and supervised the project. All authors commented on the manuscript.

Competing interests
The authors declare no competing interests.

ARTICLE IN PRESS

ARTICLE IN PRESS

FIG. 1. **Comparison between parametric solitons in degenerate OPO with hyperparametric solitons in non-degenerate OPO. a,e,** Linearly phase-matched (a) degenerate and (e) nondegenerate four-wave mixing processes. **b,f,** (b) Coexistence of the OPO and stable non-OPO regimes in the degenerate case, and (f) bistability between two distinct OPO states in the nondegenerate case. Dashed lines indicate unstable states. **c,d,g,h,** Parametric (c,d) and hyperparametric (g,h) solitons in the signal field and their respective spectra. Text in panels (a) and (e) also specifies whether the pump, A_p, signal, A_s, and idler, A_i, components fall into regions of normal ($D_2 < 0$) or anomalous ($D_2 > 0$) dispersion.

FIG. 2. **Resonator geometry, loss, dispersion, and phase matching profiles. a.** Microscope image of a ring resonator with a pulley coupler with $\theta = 25°$. **b.** Dimensions of the resonator and bus waveguide. **c.** Measured resonance with Lorentz fitting at the pump frequency of 191.4 THz, indicating a relative mode number of zero ($\mu = 0$). Q_p^{load}, Q_p^{intr} and Q_p^{coup} are the loaded (total), intrinsic and coupling quality factors, respectively. Close values of Q_p^{load} and Q_p^{coup} highlight strong over-coupling conditions. **d.** Simulated and experimental Q_p^{load} versus relative mode number (μ), showing a steep rise above $\mu = 150$ (220 THz) and a high maximum corresponding to the anti-resonance coupling condition around $\mu = -180$ (154 THz). **e, f.** Free spectra range (FSR) and frequency mismatch (Δf_μ, see Eq. (1)) versus mode number and frequency. Dispersion is normal for decreasing FSR and anomalous for increasing FSR. Circles in **c-f** show experimental points.

FIG. 3. **Frequency comb measurement setup, soliton steps, OPO, soliton spectra, and noise. a**. Experimental setup. FPC: polarisation controller; EDFA: erbium-doped fiber amplifier; BPF: band-pass filter; FBG: fiber Bragg grating; PD: photo-diode; ESA: electrical spectrum analyser; TSL: tunable semiconductor laser; DSO: digital storage oscilloscope; OSA: optical spectrum analyser. **b**. Measured OPO spectrum under an on-chip power of 250 mW. **c**. Measured OFC power when scanning the laser across the resonance at 191.4 THz for different values (375, 400, 425, 450, 475, and 500 mW) of the on-chip laser power. Green shading shows the soliton steps. The inset shows the ten repeat measurements in the 425 mW case. **d**. Three-colour spectrum of a hyperparametric single-soliton. Inset: beat note between $\mu = -6$ soliton line and TSL. **e**. The spectrum obtained by modulating the hyperparametric single-soliton with electro-optic (EO) modulators. **f, g**. RF signals of the $\mu = -1$ comb line, see shaded interval in **e**.

FIG. 4. **Numerical results for parametric CW states and hyperparametric solitons. a**. Intraresonator signal power, $|a_\mu|^2$, vs dimensionless detuning, $\delta = (f_0 - f_p)/\frac{1}{2}\kappa_0$, for six OPO states $\mu = \pm 250, \ldots, \pm 256$. $\mu = \pm 253$ OPO pair bifurcates first ($\delta \approx -2.15$) creating a bistable loop with itself; see the thick red and green lines highlighting the OPO-1 and OPO-2 states, cf. Fig. 1f. The shaded interval indicates the range of existence of hyperparametric solitons. **b**. Dimensionless intraresonator pump power, $|a_0|^2$, corresponding to the signals shown in (a). The dashed-dotted line shows the nonlinear resonance without parametric generation, i.e., for $a_{\mu\neq 0} = 0$. **c**. Three-colour output spectrum of a hyperparametric soliton computed for $\delta = -0.3215$. **d**. Numerically computed spectra for a laser frequency sweep show parametric generation of the $\mu = \pm 253$ modes at 242 THz and 141 THz, which is then replaced by 3-colour combs and hyperparametric solitons. **e**. Pulse profiles of the signal (bright soliton), pump (quasi-CW), and idler (quasi-CW) components of a hyperparametric soliton corresponding to the spectrum in (c). Pulse envelopes are computed as per Eq. (7) in Methods. Squares, diamonds, and crosses show the powers of the pump, signal, and idler components for the OPO-2 state making up the soliton background. On-chip power applied in the modelling is $\mathcal{W} = 367$mW. Scaling for the intraresonator power to use in **a,b,e** is 18.3W, see Methods.

FIG. 5. **Hyperparametric soliton crystals, quasi-crystals, multi-soliton states, and breathers. a.** Experimentally measured three-colour spectra (top to bottom) for the two-soliton crystal, two-soliton state, three-soliton crystal, four-soliton crystal, and five-, six-, and seven-breather-soliton crystals. **b.** Experimental heterodyne beat note measurements (between a comb line and TSL) for the soliton states shown in (a). Squares in the three bottom plots indicate the breather frequencies. **c.** Numerically modelled spectra of a two-soliton crystal and a four-soliton quasi-crystal. **d.** Simulated spatial profiles of signal pulses associated with the 242 THz spectra in **c**.

ARTICLE IN PRESS

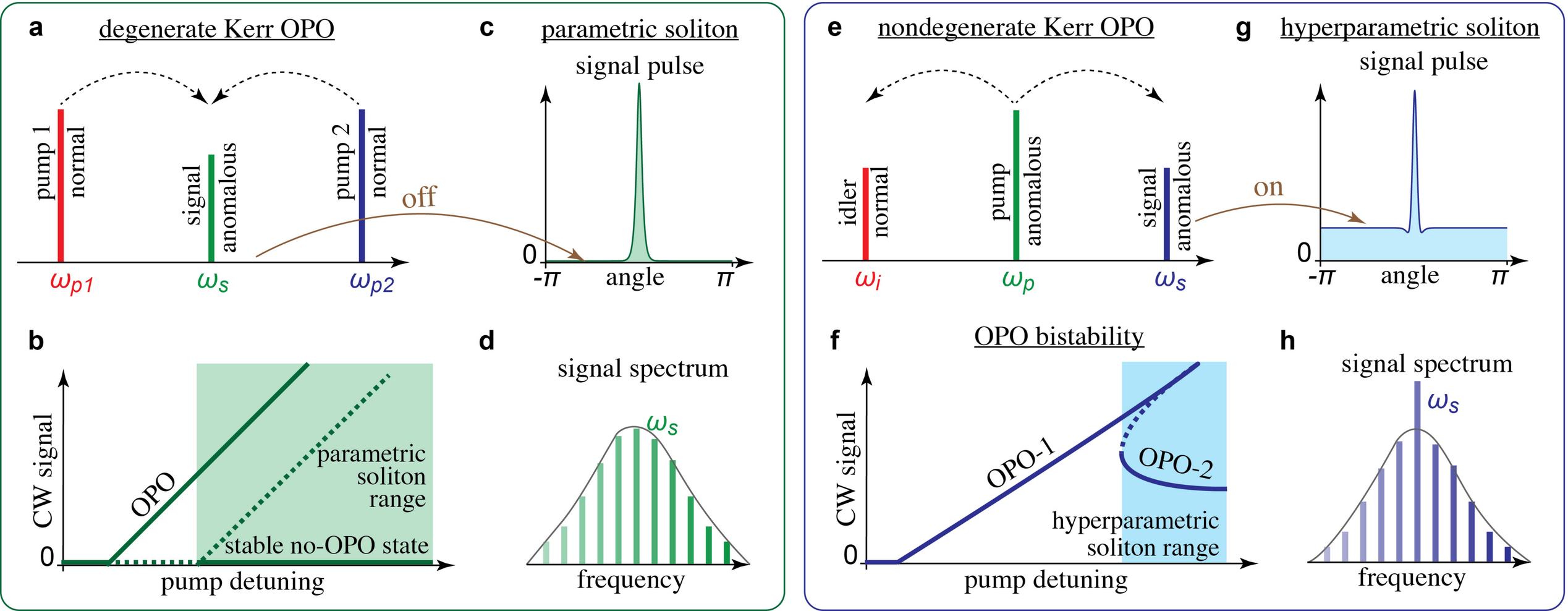
a
degenerate Kerr OPO
pump 1
normal
signal
anomalous
pump 2
normal
off
ω_{p1}
ω_s
ω_{p2}
c
parametric soliton
signal pulse
0
-π
angle
π
b
CW signal
OPO
parametric
soliton
range
stable no-OPO state
0
pump detuning
d
signal spectrum
ω_s
frequency
e
nondegenerate Kerr OPO
idler
normal
pump
anomalous
signal
anomalous
ω_i
ω_p
ω_s
g
hyperparametric soliton
signal pulse
on
0
-π
angle
π
f
OPO bistability
CW signal
OPO-1
OPO-2
hyperparametric
soliton range
0
pump detuning
h
signal spectrum
ω_s
frequency

ARTICLE IN PRESS

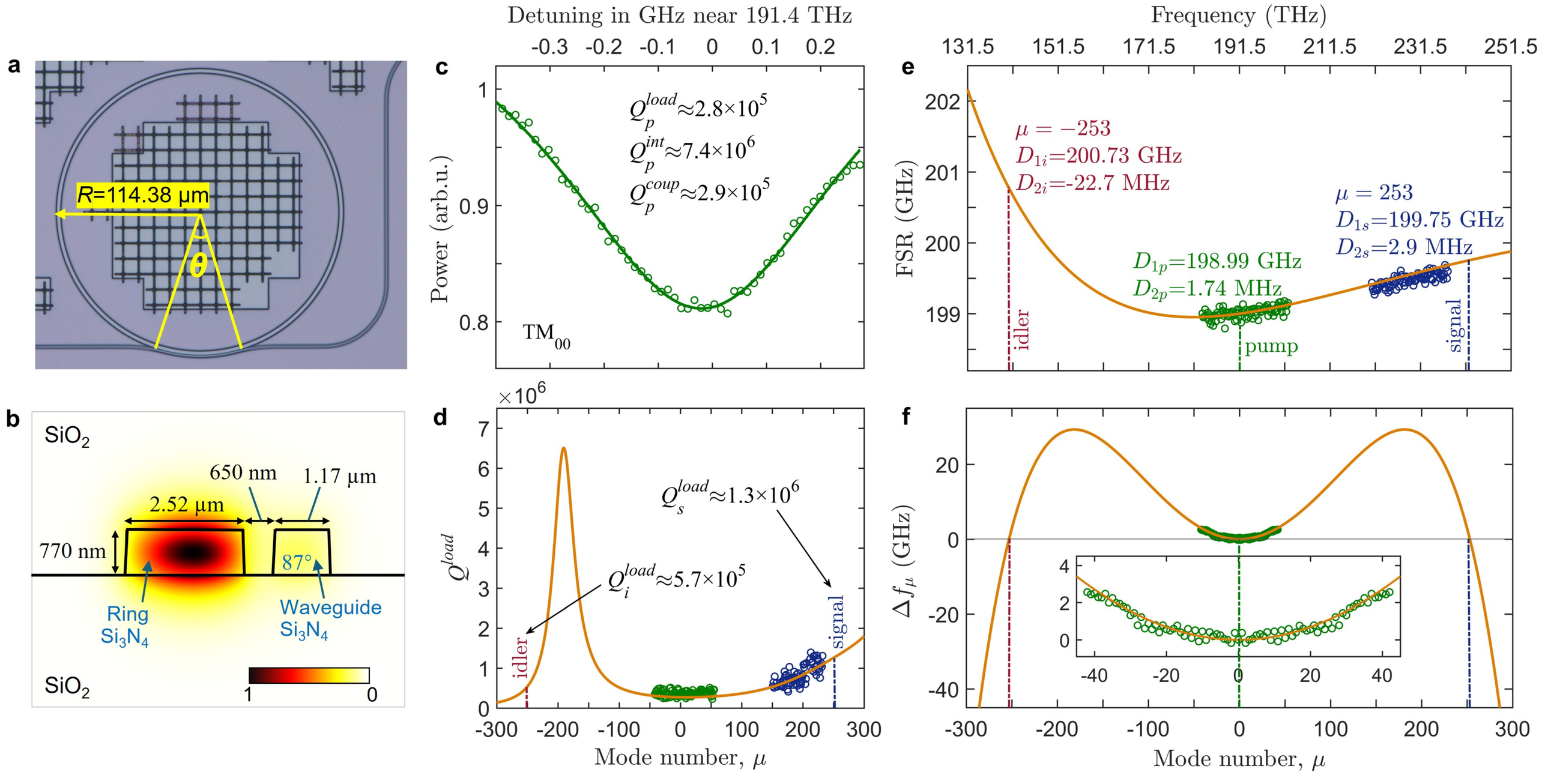

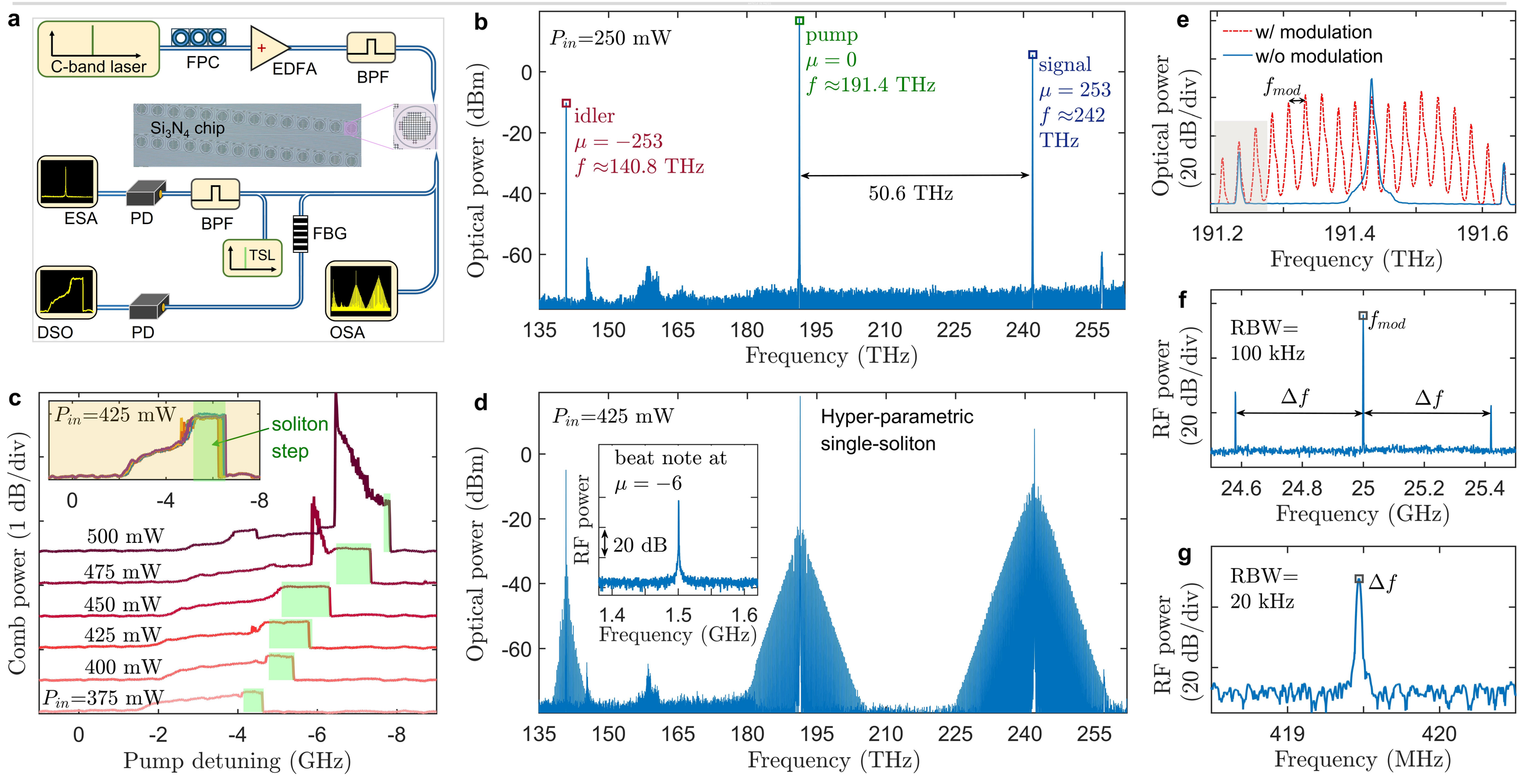
a
C-band laser
FPC
EDFA
BPF
Si3N4 chip
ESA
PD
BPF
FBG
TSL
DSO
PD
OSA
b
Pin=250 mW
pump
μ = 0
f ≈191.4 THz
signal
μ = 253
f ≈242 THz
idler
μ = −253
f ≈140.8 THz
50.6 THz
Optical power (dBm)
Frequency (THz)
c
Pin=425 mW
soliton step
500 mW
475 mW
450 mW
425 mW
400 mW
Pin=375 mW
Comb power (1 dB/div)
Pump detuning (GHz)
d
Pin=425 mW
Hyper-parametric single-soliton
beat note at
μ = −6
20 dB
RF power
Frequency (GHz)
Optical power (dBm)
Frequency (THz)
e
w/ modulation
w/o modulation
fmod
Optical power (20 dB/div)
Frequency (THz)
f
RBW= 100 kHz
fmod
Δf
Δf
RF power (20 dB/div)
Frequency (GHz)
g
RBW= 20 kHz
Δf
RF power (20 dB/div)
Frequency (MHz)

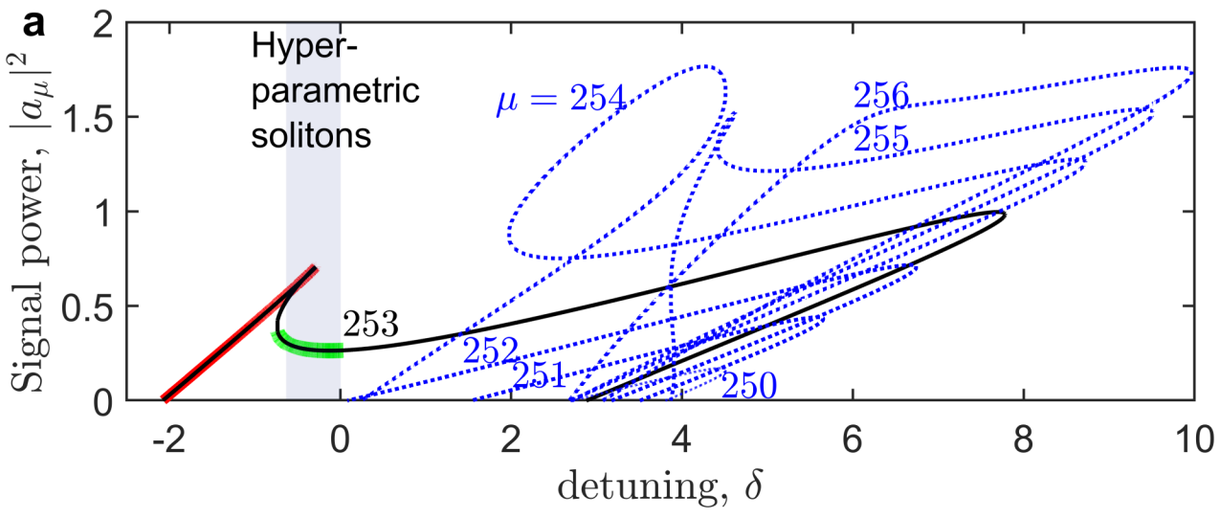
a
Hyper-
parametric
solitons
$\mu = 254$
256
255
253
252
251
250
Signal power, $|a_\mu|^2$
detuning, δ

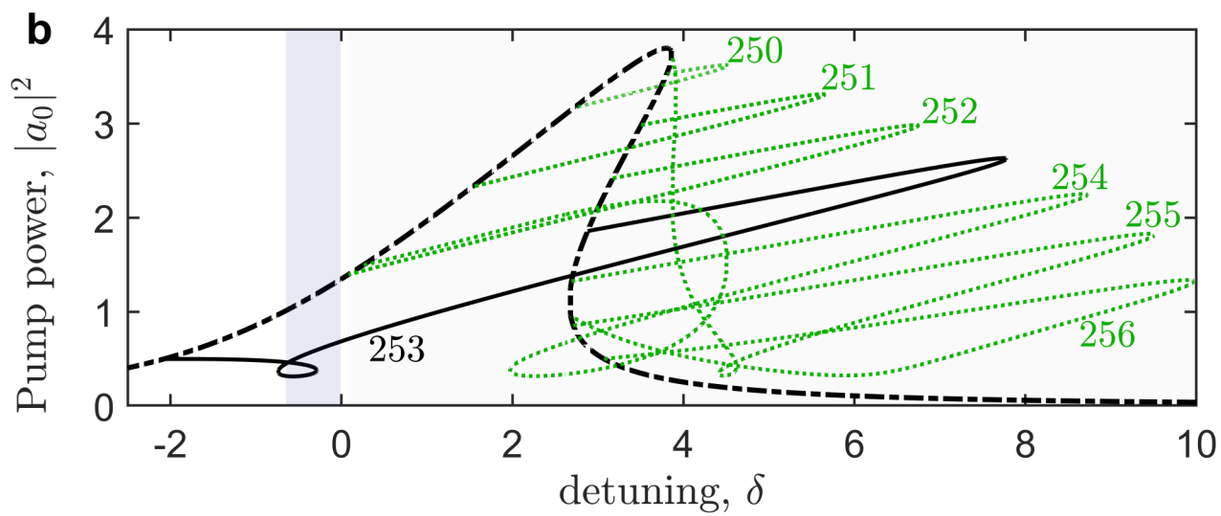
b
250
251
252
254
255
253
256
Pump power, $|a_0|^2$
detuning, δ

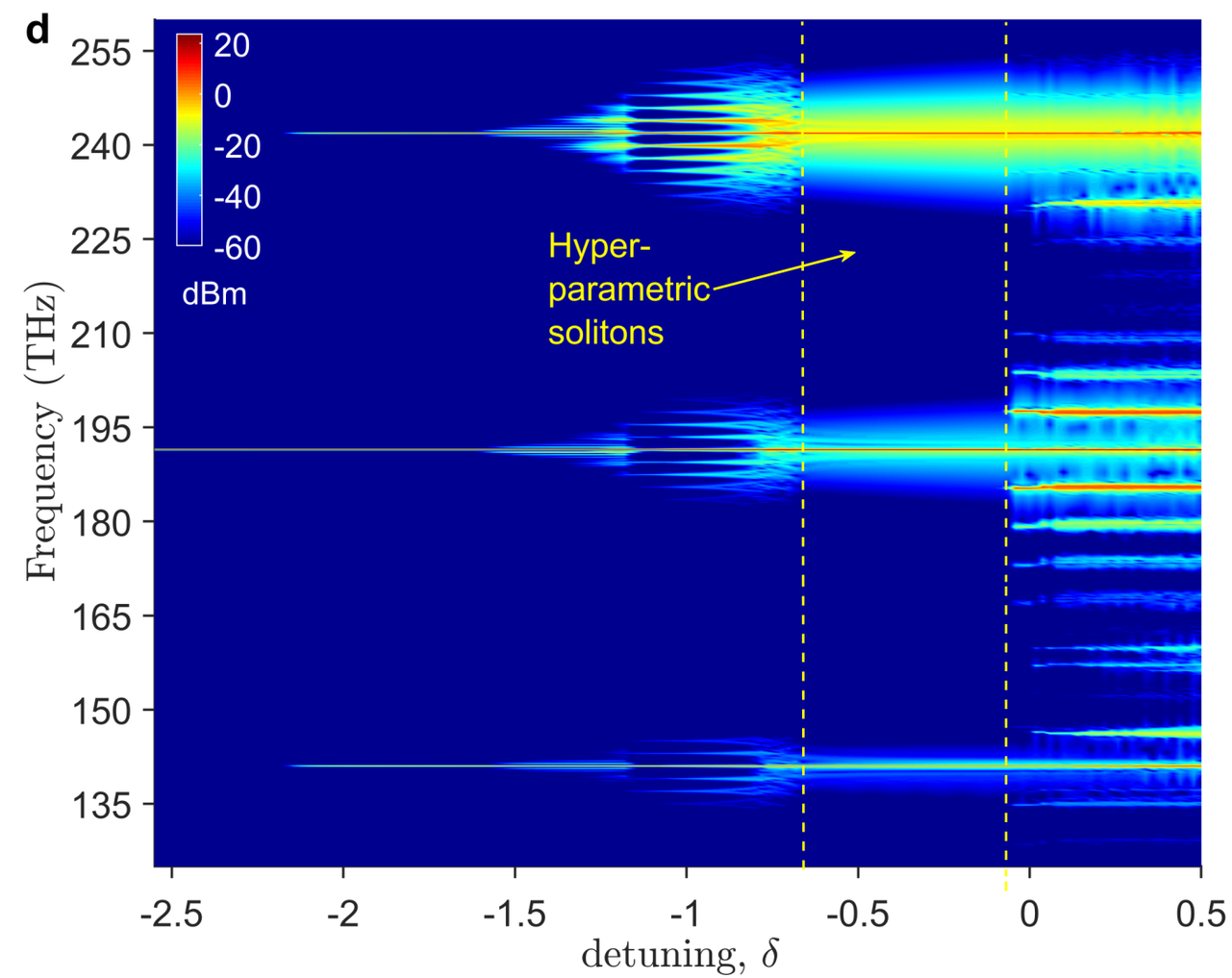
d
20
0
-20
-40
-60
dBm
Hyper-
parametric
solitons
Frequency (THz)
detuning, δ

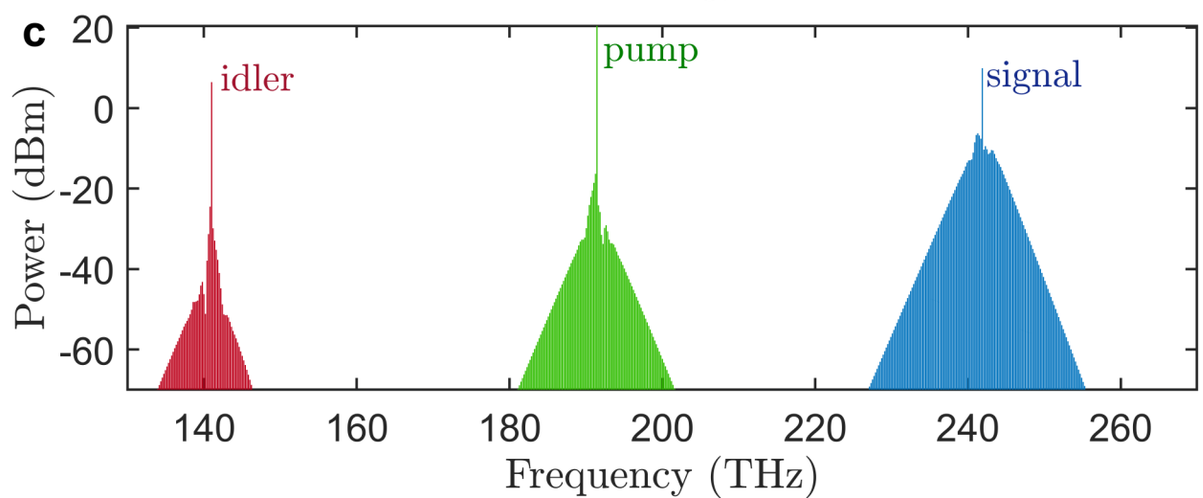
c
idler
pump
signal
Power (dBm)
Frequency (THz)

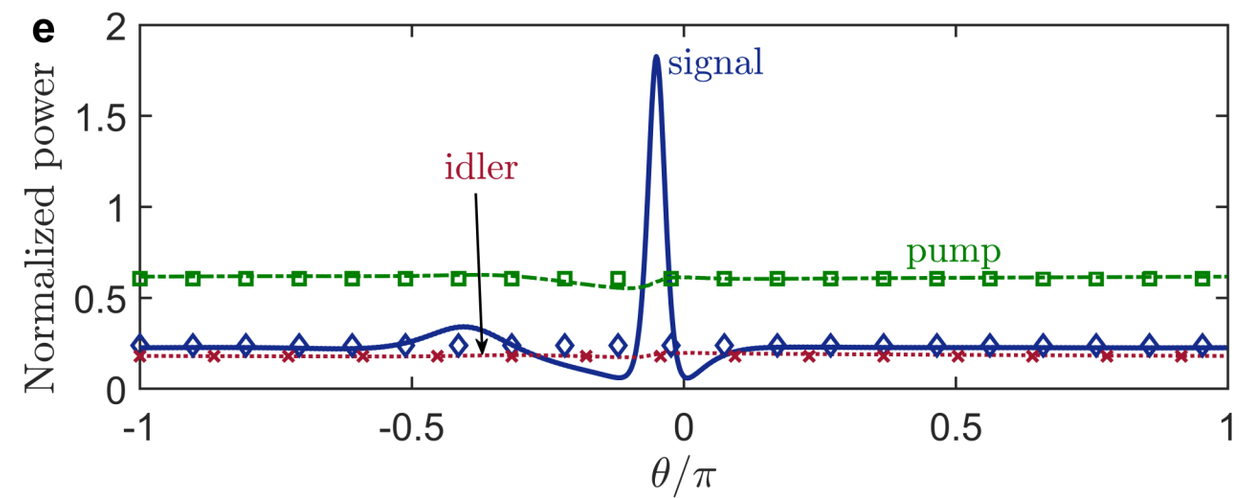
e
signal
idler
pump
Normalized power
θ/π

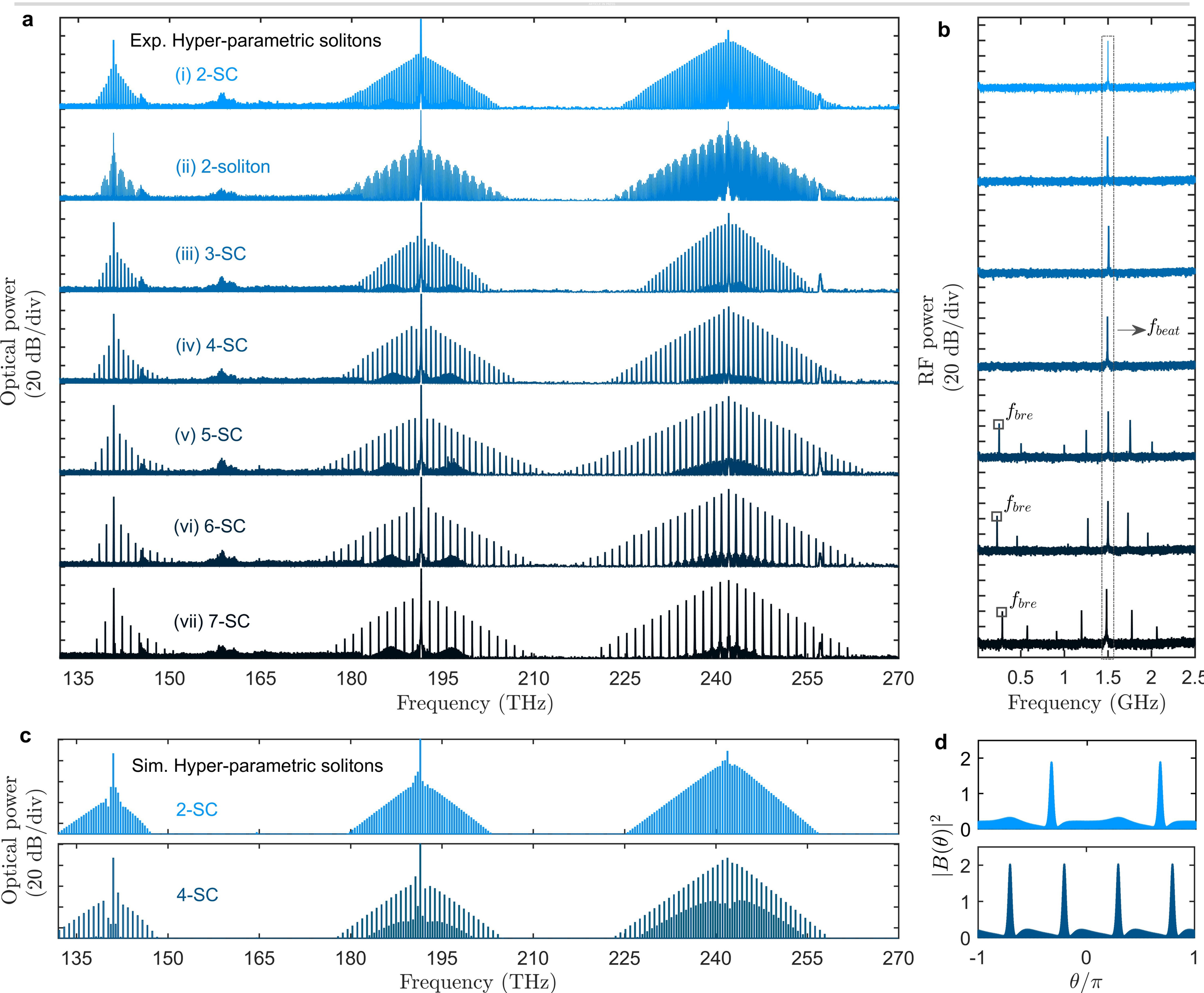
a
Exp. Hyper-parametric solitons
(i) 2-SC
(ii) 2-soliton
(iii) 3-SC
(iv) 4-SC
(v) 5-SC
(vi) 6-SC
(vii) 7-SC
Optical power (20 dB/div)
135
150
165
180
195
210
225
240
255
270
Frequency (THz)
b
RF power (20 dB/div)
f_{beat}
f_{bre}
f_{bre}
f_{bre}
0.5
1
1.5
2
Frequency (GHz)
c
Sim. Hyper-parametric solitons
2-SC
4-SC
Optical power (20 dB/div)
135
150
165
180
195
210
225
240
255
270
Frequency (THz)
d
$|B(\theta)|^2$
2
1
0
-1
0
1
θ/π